

# Exploitation of hydrate reservoirs using CO<sub>2</sub> injection. Experimental studies and theoretical modelling

Kvamme<sup>1</sup>, Gránásy<sup>2</sup>, L, B., Graue<sup>1</sup>, A., Kuznetsova<sup>1</sup>, T., Svandal<sup>1</sup>, A.

<sup>1</sup> University of Bergen, Bergen, Norway

<sup>2</sup> Research Institute for Solid State Physics and Optics, Budapest, Hungary

## Abstract.

Formation and dissociation of gas hydrates have been imaged in a sandstone core plug using Magnetic Resonance Imaging (MRI). This paper describes the experimental procedures developed to form CO<sub>2</sub> and methane hydrates in sandstone rock while monitoring the process with MRI. MRI was found to provide excellent resolution between the hydrate and its liquid/gas precursors and allowed the dynamic, spatial imaging of the formation and dissociation of hydrates under various injection conditions. A phase field theory is applied to describe the formation of CO<sub>2</sub> hydrate in aqueous solutions. Starting from realistic estimates for the thermodynamic and interfacial properties, we show that under typical conditions of CO<sub>2</sub> formation, the size of the critical fluctuations (nuclei) is comparable to the interface thickness, implying that the classical droplet model, which relies on a sharp interface, is rather inaccurate. The phase field theory predicts considerably smaller nucleation barrier than the classical approach and converges, as expected, to the classical prediction with decreasing interface thickness. We determine the dimensionless growth rate of small CO<sub>2</sub> hydrate clusters in aqueous solution. Finally, we explore the possibility to model solidification in porous matter and liquid channel using the phase field theory.

## Introduction

The total energy corresponding to natural gas entrapped in hydrate reservoirs might be more than twice the energy of all known sources of coal and hydrocarbons. The thermodynamic stability of carbon dioxide hydrate is significantly higher than the corresponding stability of natural gas hydrate at typical reservoir conditions of temperature and pressure. Injection of carbon dioxide into hydrate reservoirs will therefore lead to conversion from natural gas hydrate to carbon dioxide hydrate. Transformation of natural gas hydrate to carbon dioxide hydrate will therefore represent a safe, stable, long term, storage option for carbon dioxide, while at the same time releasing natural gas. There is even an energy gain in the order of 20% during the transformation from natural gas hydrate over to CO<sub>2</sub> hydrate. The world wide focus on reduction of carbon dioxide emissions to the atmosphere has resulted in a corresponding focus on different options for storage of carbon dioxide. Storage of carbon dioxide is normally considered to be a cost. Replacement of natural hydrate by CO<sub>2</sub> hydrate will reduce the net cost of the CO<sub>2</sub> storage due to the value of the released natural gas. If we as an example use the present hydrate resources in the Storegga slide it covers an area of 4000 km<sup>2</sup> [16]. The hydrate layers in this area vary between 40 and 50 meters thickness. The content of the hydrate in this area may vary between 2 and 10%, which corresponds on the average to  $1.80 \cdot 10^{12}$  m<sup>3</sup> natural gas referred to standard conditions. The corresponding storage capacity for CO<sub>2</sub> is  $1.3 \cdot 10^{12}$  standard m<sup>3</sup>. For comparison the injection of CO<sub>2</sub> from the Sleipner field, into the Utsira formation, is  $5.6 \cdot 10^8$  standard m<sup>3</sup> per year. Replacement of natural gas hydrate with CO<sub>2</sub> hydrate will also significantly increase the hydrate stability region in terms of temperature and pressure and thus reduce the risk of future catastrophic dissociation scenarios. Another situation is the potential role of hydrate in different scenarios related to storage of carbon dioxide in aquifers. Outside the northern coast of Norway seafloor temperatures may well be below zero. Storage of CO<sub>2</sub> in reservoirs in these regions may thus very well imply regions of hydrate stability. Formation of hydrate films may reduce the leakage fluxes from these reservoirs.

The advantage of hydrate reservoir exploitation using CO<sub>2</sub> injection, versus heat injection and/or pressure reduction, is the economics. The kinetics of natural gas hydrate reservoir exploitation using CO<sub>2</sub> injection is, however, not well known due to the large variety in properties of solid material and limited possibilities for fundamental experimental techniques that can explore the finer details of the conversion process.

In this work we present a concept of experiments and theoretical simulations. Magnetic Resonance Imaging (MRI) is used to image the progress of hydrate formation, hydrate dissociation and hydrate reformation in porous medium under realistic conditions in 3D on a sub millimeter scale. Similar theoretical model systems describing the kinetics of the phase transitions are constructed using the Phase Field Approach [2, 3]. The final step is a simplification of the results into a form suitable form [3] for use in a large scale reservoir simulator.

### Experimental

Formation and disassociation of carbon dioxide ( $\text{CO}_2$ ) and methane ( $\text{CH}_4$ ) hydrates were first studied in bulk phase to experimentally identify temperature and pressure conditions for the hydrate formation and disassociation processes. Formation and disassociation of gas hydrates were then imaged in a sandstone core plug using MRI tomography. Applying MRI tomography allowed dynamic in-situ imaging of the formation and melting of hydrates under various injectivity conditions. A cooling system capable of holding a core holder at a desired stable temperature within the range of  $0\text{--}15^\circ\text{C}$ , with an accuracy of  $0.1^\circ\text{C}$ , for an extended period of time was constructed. The cooling fluid selected, Fluorinert (FC-84), needed to be invisible for MRI and was also used as fluid for the confinement pressure in the core holder. The tubing for the cooling fluid was embedded in plastic tubing filled with an antifreeze fluid, circulating between two cooling baths, which was not piped through the MRI. The core holder was made of a composite material to minimize influence on the imaging capabilities. Figure 1 shows a schematic drawing of the MRI set up. An image of a cross section of the core is shown in fig. 2.

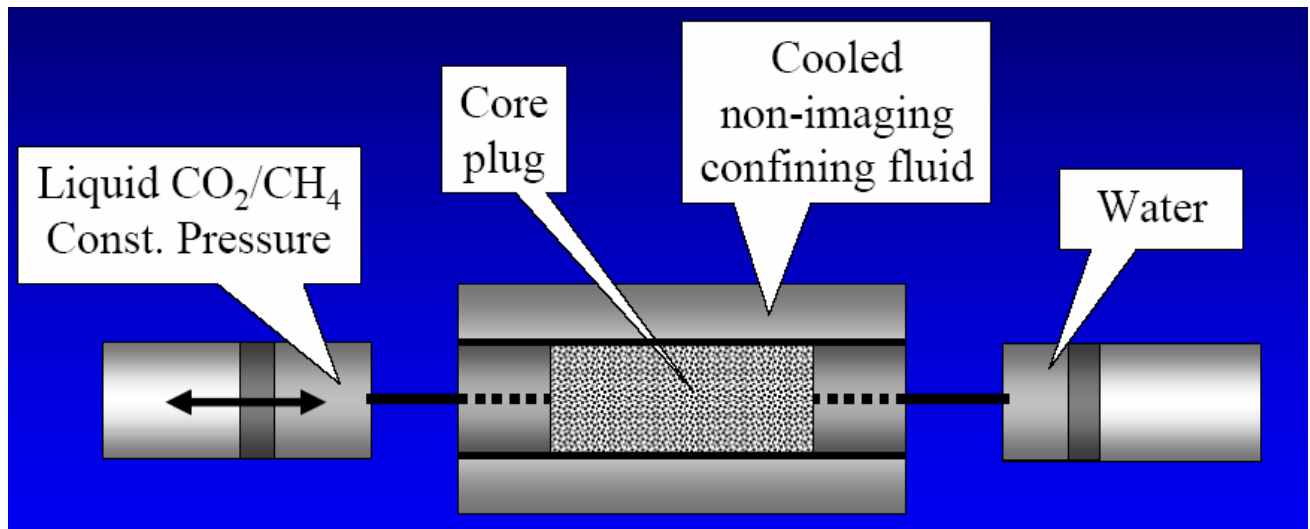


Fig. 1. Schematic drawing of the MRI setup with supply system for water and methane or  $\text{CO}_2$ . The core holder is immersed in a cylinder containing the cooling fluid that keeps the system at constant temperature.

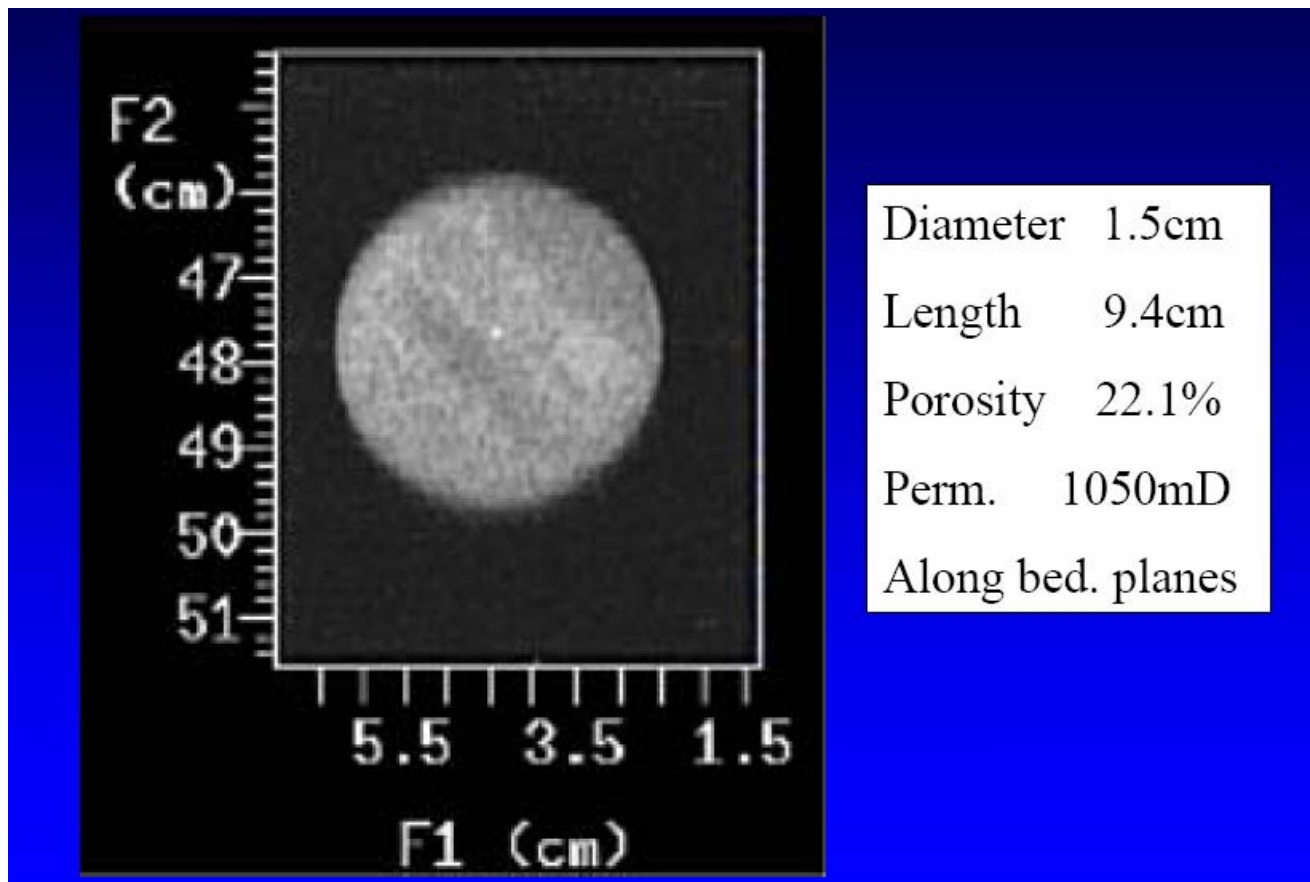
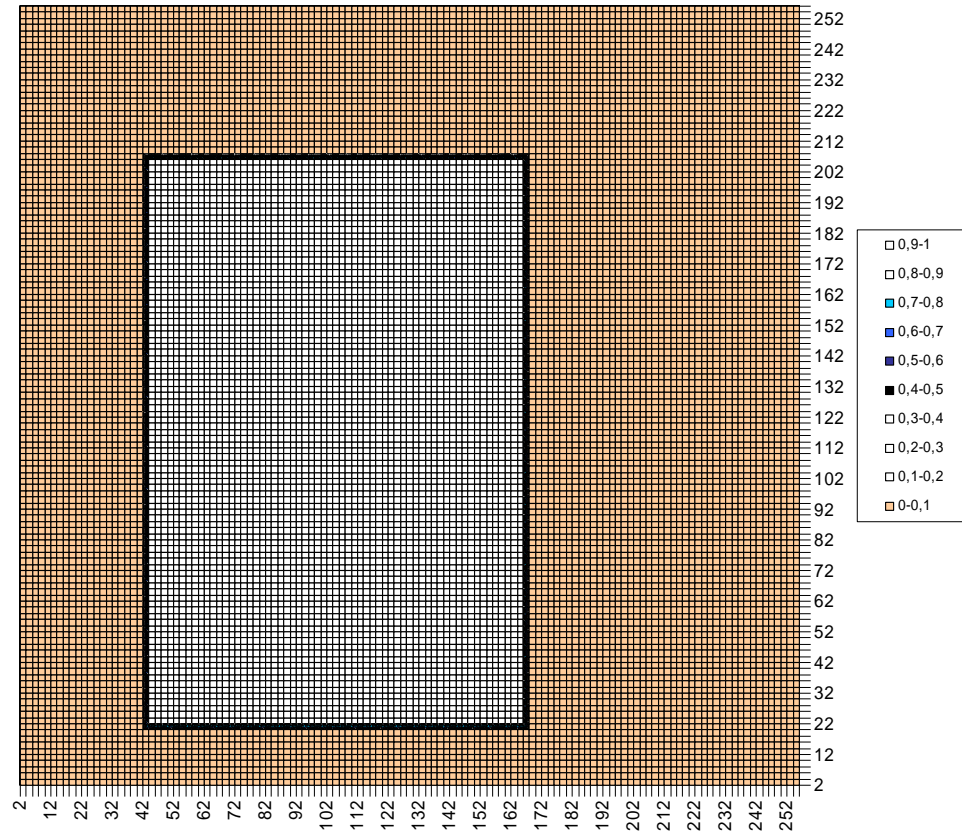


Fig. 2. A cross section image of the core and some basic data of the core.

The core length is 9.4 cm and the core diameter is 1.5 cm. Porosity was measured at 22.1% and the brine permeability at 1050 mD.

The core was saturated with brine, placed inside the core holder in the MRI tomograph and pressurized applying 80 bars confinement pressure. In an attempt to reproduce conditions that are, or would be, present in nature, i.e. gas with water present, a gas-water displacement process was initiated. A liquid gas phase, CO<sub>2</sub> at 63 bars and 25 °C, was introduced at one end of the 100% brine saturated core sample. The liquid gas-water displacement was imaged. The core holder was then cooled to 2.0 °C and hydrate began to form. Imaging the change in the free water saturation as function time provides an indirect measure of the hydrate formation and disassociation during temperature variations.

Fig. 3 shows 2D projections of the conversion of water into hydrate. With the imaging technique the hydrate water is invisible. The relative conversion over to hydrate can thus be traced by the liquid water intensity of the different sections of the core. 3 a) shows the initial imaging, reflecting the signal for liquid water. 3 b) is the image after the temperature was lowered to 2 C. 3 c) is an images fter 30 minutes and 3 d) a corresponding image after 8 hours. As can be seen in the figure the hydrates started to form in the areas of highest gas saturation. The results show that hydrate took several hours to form and formed according to the gradually decreasing gas saturation from the gas injection face rather than in discrete areas. The gas phase was continuous from the injection face throughout the 9 cm long sample and the hydrates formed everywhere. The hydrate formed with a gradually decreasing distribution from the gas injection face rather than in discrete areas, within the experimental resolution of ca 0.4 mm. Permeability went to zero when less than half of the sample was filled with hydrate implying that selected, but not detected, areas were completely filled with hydrate before all of the pore volume was filled.



**Fig. 3 a)** 2-D MRI initial image of core at time zero (liquid state fluids only)

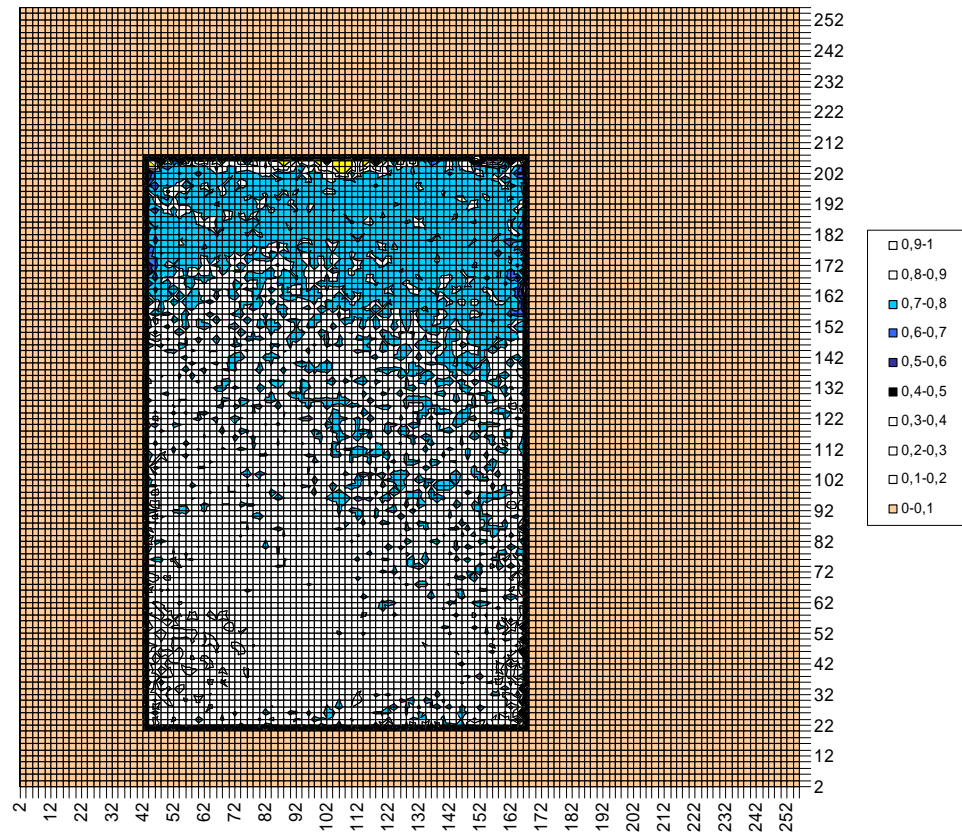


**Fig. 3 b)** 2-D MRI image after cooling to 2 C.

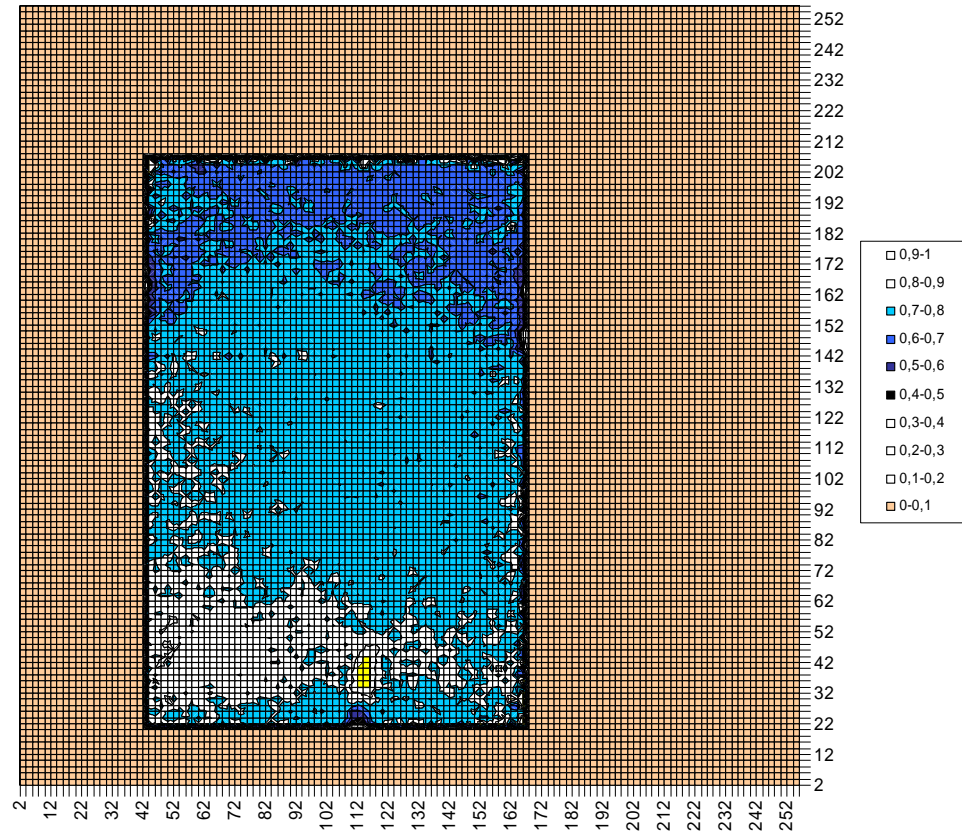


**Fig. 3 c)** 2-D MRI image after 30 minutes

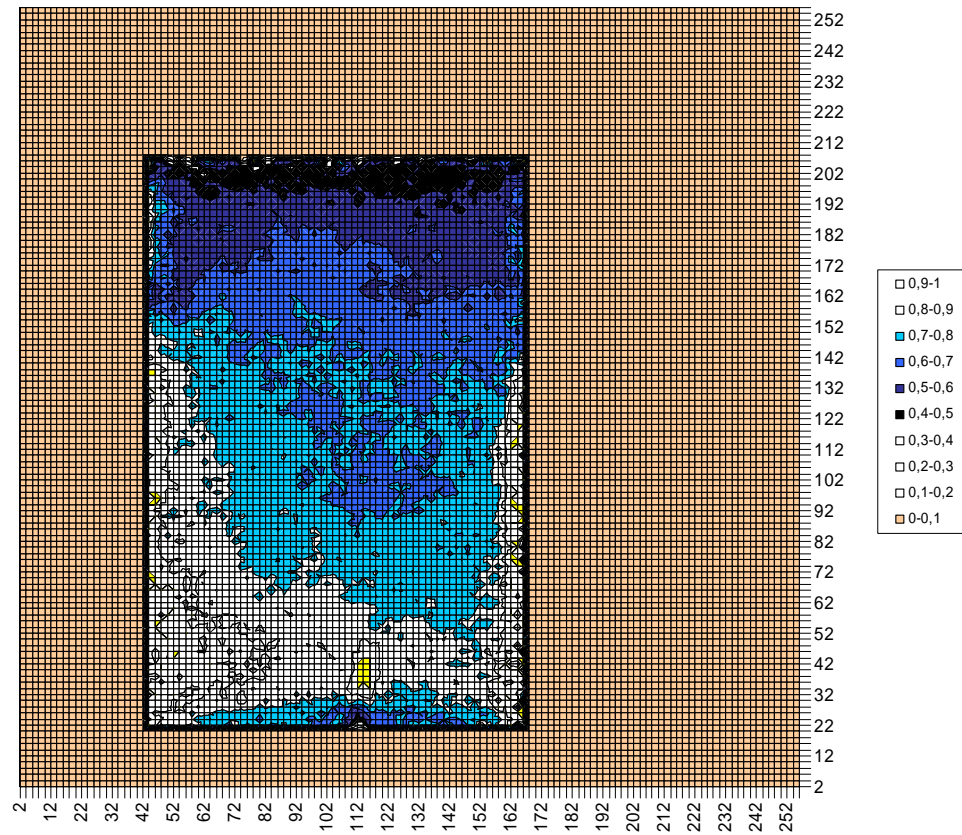


**Fig. 3 d)** 2-D MRI image after 8 hours

Heating and cooling the system several times the formation and disassociation of hydrates were monitored as function of time.

Finally, also methane was used as the gas phase. Similar experimental procedures were performed as for the CO<sub>2</sub> injection.

## Modelling nucleation and growth of hydrate

The freezing of homogeneous undercooled liquids starts with heterophases whose central part shows crystal-like atomic arrangement. The driving force for these fluctuations are thermodynamic differences between the new crystal and the parent phase(s). The free energy gain of phase transition competes with the penalty of the corresponding work exposed on the surroundings. In the classical approach there is a sharp inter-phase between the old and new phases. The corresponding critical size of a new phase is directly given by the transition where the free energy gains dominates the further development. The critical size is thus estimated from the derivative of the volumetric free energy, which should be zero at critical size. Unfortunately only a limited number of systems exhibits an interphase that is close to examples are gas/liquid phase transitions at low pressures. Other systems exhibit interphasial thickness in the order of the range of critical fluctuations and may be in the order of nanometers [4]. Therefore, the droplet model of the classical nucleation theory, which relies on a sharp interface and bulk crystal properties, is inappropriate for such fluctuations. Field theoretic models, that predict a diffuse interface, offer a natural way to handle such a situation [5]. For example, in recent works, the phase field theory has been shown to describe such fluctuations quantitatively [6,7,8]. In this work we divide the problem into a first phase where we estimate the critical nuclei of a hydrate crystal forming from dissolved CO<sub>2</sub> in aqueous solution. The theoretical details for these calculations are described in the next section. The critical particle is then immersed in a cubic box of sides 400 nm, with a division in discrete volume elements and studied for growth rates. The details are described in the subsequent section.

## Phase field theory of nuclei

Our starting point is the standard phase field theory of binary alloys as developed by several authors [6,16]. In the present approach, the local state of the matter is characterized by two fields; a structural order parameter,  $\phi$ , called the *phase field*, that describes the transition between the disordered liquid and ordered crystalline structures, and a conserved field, the coarse-grained solute concentration,  $c$ .

The structural order parameter can be viewed as the Fourier amplitude of the dominant density wave of the time averaged singlet density in the solid. If the density peaks in the solid can be well approximated by Gaussians placed to the atomic sites, all Fourier amplitudes can be expressed uniquely in terms of the amplitude of the dominant wave, thus a single structural order parameter suffices. Here we take  $m = 0$  in the solid and  $m = 1$  in the liquid. We assume mass conservation, which implies that the integral of the conservative fields over volume is a constant.

The free energy of the system is a functional of these fields:

$$F = \int d^3r \left\{ \frac{1}{2} \varepsilon^2 T (\nabla m)^2 + f(m, c) \right\}, \quad (1)$$

where  $\varepsilon$  is a constant,  $T$  is the temperature, and  $f(m, c)$  is the local free energy density. The first term on the right hand side is responsible for the appearance of the diffuse interface. The local free energy density has the form  $f(m, c) = wT [g(m) + [1 - p(m)] f_S(c) + p(m) f_L(c)]$ , where the “double well” and “interpolation” functions have the forms  $g(m) = \frac{1}{4} m^2 (1 - m)^2$  and  $p(m) = m^3 (10 - 15m + 6m^2)$ , respectively, that emerge from the thermodynamically consistent formulation of the PFT,  $w$  is the free energy scale, while the free energy densities of the homogeneous solid and liquid,  $f_S$  and  $f_L$ , depend on the local value of  $c$ . These relationships result in a free energy surface that has two minima, whose relative depth depends on the deviation from equilibrium.

Being in unstable equilibrium, the critical fluctuation (the nucleus) can be found as an extremum of this free energy functional [6,7,8], subject to the solute conservation constraint discussed above. To impose this constraint one adds the volume integral over the conserved field times a Lagrange multiplier,  $\lambda$ , to the free energy:  $\lambda \int d^3r c(\mathbf{r})$ . The field distributions, that extremize the free energy, have to obey the appropriate Euler-Lagrange (EL) equations, which in the case of such local functional take the form

$$\begin{aligned}\frac{\delta F}{\delta m} &= \frac{\partial \psi}{\partial m} - \nabla \frac{\partial \psi}{\partial \nabla m} = 0 \\ \frac{\delta F}{\delta c} &= \frac{\partial \psi}{\partial c} - \nabla \frac{\partial \psi}{\partial \nabla c} = 0\end{aligned}\tag{2}$$

where  $\delta F/\delta m$  and  $\delta F/\delta c$  stands for the first functional derivative of the free energy with respect to the fields  $m$  and  $c$ , respectively while  $\psi$  is the total free energy density. The EL equations have to be solved assuming that unperturbed liquid exists in the far field, while, for symmetry reasons zero field gradients exist at the center of the fluctuations. Under such conditions, the Lagrange multiplier can be identified as  $\lambda = -(\partial \psi/\partial c)_{r \rightarrow \infty}$ .

Assuming spherical symmetry that is reasonable considering the low anisotropy of the crystal-liquid interface at small undercoolings, the EL equations take the following form:

$$\varepsilon^2 T \left\{ \frac{d^2 m}{dr^2} + \frac{2}{r} \frac{dm}{dr} \right\} = w T g'(m) + p'(m) \{f_L - f_S\},\tag{3a}$$

and

$$0 = w T g(m) + [1 - p(m)] \frac{\partial f_S}{\partial c} + p(m) \frac{\partial f_L}{\partial c} - \frac{\partial f_L}{\partial c} \Big|_{r \rightarrow \infty}.\tag{3b}$$

Here ' stands for differentiation with respect to the argument of the function. The last term in eqn. (3b) originates from the Lagrange multiplier. Since the right hand side of eqn. (3b) is a function of fields  $c$  and  $m$ , it provides the implicit relationship  $c = c(m)$ . Accordingly, eqn. (3a) is an ordinary differential equation for  $m(r)$ . This equation has been solved here numerically using a fourth order Runge-Kutta method. Since  $m$  and  $dm/dr$  are fixed at different locations, the central value of  $m$  that satisfies  $m \rightarrow m_\infty = 1$  for  $r \rightarrow \infty$ , has been determined iteratively. Having determined the solutions  $m(r)$  and  $c(r)$ , the work of formation of the nucleus  $W^*$  can be obtained by inserting the solution into the free energy functional. Provided that the bulk free energy densities,  $f_S(c)$  and  $f_L(c)$ , are known, the only model parameters, we need to fix to evaluate  $W^*$ , are  $w$  and  $\varepsilon$ . These model parameters are related to the interface thickness and the interfacial free energy [6,19], thus these quantities can be used to determine  $w$  and  $\varepsilon$ , and calculate  $W^*$  *without adjustable parameters*.

The steady state nucleation rate (number of nuclei formed in unit volume and time),  $J_{SS}$ , can be calculated as

$$J_{SS} = J_0 \exp \left\{ -W^* / kT \right\},\tag{4}$$

using the classical nucleation prefactor [20],  $J_0$ , verified experimentally on oxide glasses [21].

### ***Phase field theory of polycrystalline growth***

To address hydrate crystallization and polycrystalline growth, we rely on an extension of the phase field theory developed recently [6,7,9], which relies on the orientation field,  $\theta$ , first introduced by Kobayashi, Warren and Carter [10]. This field specifies the local orientation of the crystal planes in the laboratory system, and allows the description of polycrystalline solidification and grain boundary evolution. It is normalized so that it varies between 0 and 1, while the orientation angle covers 0 and  $2\pi/n$ , where  $n$  is the symmetry index (e.g.,  $n = 6$  applies for six-fold symmetry). In order to handle nucleation of crystallites with different crystallographic orientations, we assume that  $\theta$  fluctuates in space and time. This extension of the orientation field to the liquid phase captures the short-range order existing in the liquid. The orientation field is strongly coupled to the phase field so that structural and orientational changes take place simultaneously at the crystal-liquid interface. This coupling is realized by adding an orientational contribution to the free energy functional.

$$F = \int d^3r \left\{ \frac{1}{2} \varepsilon^2 T (\nabla m)^2 + f(m, c) + f_{ori}(m, \nabla \theta) \right\}, \quad (5)$$

where  $f_{ori}(m, \nabla \theta) = [1 - p(m)]HT |\nabla \theta|$  is the driving force for orientational ordering, and  $H$  is a constant.

The equations of motion for the three fields are

$$\begin{aligned} \dot{\phi} &= -M_m \frac{\delta F}{\delta m} = M_m \left\{ \nabla \left( \frac{\partial f}{\partial \nabla m} \right) - \frac{\partial f}{\partial m} \right\} + \zeta_m \\ \dot{c} &= \nabla M_c \nabla \frac{\delta F}{\delta c} = \nabla \left\{ Dc(1-c) \nabla \left[ \left( \frac{\partial f}{\partial c} \right) - \nabla \left( \frac{\partial f}{\partial \nabla c} \right) \right] \right\} + \zeta_j \\ \dot{\theta} &= -M_\theta \frac{\delta F}{\delta \theta} = M_\theta \left\{ \nabla \left( \frac{\partial f}{\partial \nabla \theta} \right) - \frac{\partial f}{\partial \theta} \right\} + \zeta_\theta \end{aligned} \quad (6)$$

Here  $\zeta_i$  ( $i = m, j, \theta$ ) are Langevin noise terms for the two non-conserved fields  $m$  and  $\theta$ , and for the concentration flux  $j$ , that model the thermal fluctuations in the system. Introducing the time scale  $\tau = \xi^2 / D_l$ , where  $\xi$  is a length scale and  $D_l$  the diffusion coefficient of the liquid, the following dimensionless forms emerge for the deterministic part of the equations of motion:

$$\begin{aligned} \tilde{m} &= \frac{M_m \varepsilon^2 T}{D_l} \left[ \tilde{\nabla} (s^2 \tilde{\nabla} m) - \frac{\partial}{\partial \tilde{x}} \left\{ s \frac{\partial s}{\partial \mathcal{G}} \frac{\partial m}{\partial \tilde{y}} \right\} + \frac{\partial}{\partial \tilde{y}} \left\{ s \frac{\partial s}{\partial \mathcal{G}} \frac{\partial m}{\partial \tilde{x}} \right\} \right. \\ &\quad \left. - \xi^2 \frac{w(c)Tg'(m) + p'(m) \left\{ f_L(c, T) - f_S(c, T) - HT |\tilde{\nabla} \theta| / \xi \right\}}{\varepsilon^2 T} \right] \\ \tilde{c} &= \tilde{\nabla} \left\{ \frac{v_m}{RT} \lambda c(1-c) \tilde{\nabla} \left[ (w_B - w_A)Tg(m) + [1 - p(m)] \frac{\partial f_S}{\partial c}(c, T) \right] \right. \\ &\quad \left. + p(m) \frac{\partial f_L}{\partial c}(c, T) \right\} \\ \tilde{\theta} &= \chi \left[ \tilde{\nabla} \left\{ [1 - p(m)] \frac{\tilde{\nabla} \theta}{|\tilde{\nabla} \theta|} \right\} - \frac{\varepsilon^2}{H\xi} s \frac{\partial s}{\partial \theta} |\tilde{\nabla} \phi|^2 \right]. \end{aligned}$$



where tilde denotes differentiation with respect to dimensionless quantities. Here  $M_c = (v_m/RT) D c (1 - c)$  is the mobility of the concentration field,  $v_m$  the average molar volume,  $D = D_s + (D_l - D_s) p(m)$  is the diffusion coefficient, and  $\lambda = D/D_l$  is the reduced diffusion coefficient, while  $\chi = M_\theta \xi HT / D_l$  is the dimensionless orientational mobility. Note a second term on the RHS of the equation for the orientation field included recently [6].

In this work, these equations were solved numerically using an explicit scheme and MPI protocol on a PC cluster consisting of 56 nodes, built up in the Research Institute for Solid State Physics and Optics, Budapest. A periodic boundary condition is applied at the borders of the simulation window, unless stated otherwise.

To study solidification in a confined space, we introduce “walls”, where the normal component of  $\nabla m$  and  $\nabla c$  are set zero (“no flux” boundary condition). The former ensures a 90 degrees contact angle, while the latter realizes a chemically inert wall.

### **Material properties**

The molar Gibbs free energy of the aqueous CO<sub>2</sub> solution has been calculated as  $G_L = (1 - c) G_{L,W} + c G_{L,CO_2}$ , where  $c$  is the mole fraction of CO<sub>2</sub>. The partial molar Gibbs free energy of water in solution has been obtained as  $G_{L,W} = G_{L,W}^0 + RT \ln[(1 - c) \gamma_{L,W}(c)]$ , where the free energy of pure water has been calculated as

$$G_{L,W}^0 = \sum_{i=0}^3 \frac{k_i}{T^i}, \quad (7)$$

with coefficients  $k_i$  taken from Ref. 25. Here  $R$  is the gas constant and  $\gamma_{L,W}$  is the activity coefficient of water in solution. The partial molar free energy of CO<sub>2</sub> in solution is  $G_{L,CO_2} = G_{L,CO_2}^\infty + RT \ln[c \gamma_{L,CO_2}(c)]$ , where the molar free energy of CO<sub>2</sub> at infinite dilution,  $G_{L,CO_2}^\infty = -19.67$  kJ/mol, has been taken from molecular dynamics simulations [12]. The temperature and pressure dependent activity coefficient of CO<sub>2</sub> in aqueous solution deduced from CO<sub>2</sub> solubility experiments of Stewart and Munjal [13] have been fitted using the form

$$\ln \gamma_{L,CO_2} = \sum_{i=0}^5 a_i(T) [\ln x]^i, \quad (8)$$

with  $a_i(T)$  given by third order polynomials. The activity coefficient of water,  $\gamma_{L,W}$  in aqueous solution has been obtained from eqn. (6) via the Gibbs-Duhem relationship.

The Gibbs free energy of the hydrate is given by  $G_S = (1 - c)G_{S,W} + cG_{S,CO_2}$ . Owing to the lack of experimental information, the partial molar quantities have been calculated using the model described in Ref. 25. For water and CO<sub>2</sub> we use the relationships  $G_{S,W} = G_{S,W}^0 + RT (3/23) \ln(1 - \theta)$ , and  $G_{S,CO_2} = G_{S,CO_2}^{inc} + RT \ln[\theta/(1 - \theta)]$ , respectively, where the hole occupancy is  $\theta = c/(3/23)$ . Here, the partial molar Gibbs free energies of the empty clathrate,  $G_{S,W}^0$ , and that of guest inclusion,  $G_{S,CO_2}^{inc}$ , are given by eqn. (6), with the appropriate  $k_i$  taken from Ref. 14.

Following other authors [15], we approximate the free energy of the hydrate-solution interface by that of the ice-water interface, taken from the work of Hardy,  $29.1 \pm 0.8$  mJ/m<sup>2</sup> [16]. Owing to a lack of information on the CO<sub>2</sub> hydrate/aqueous solution interface, we use the 10% – 90% interface thickness,  $d$ , (the distance on which the phase field changes between 0.1 and 0.9) as an adjustable parameter in the calculations. Molecular dynamics simulations on other clathrate hydrates indicate that the full interface thickness is about 2 – 3 nm [17], that corresponds to roughly  $d \approx 1 - 1.5$  nm. Assuming that similar values apply for the CO<sub>2</sub> hydrate, we vary  $d$  in the 0.125 – 1.5 nm range. Indeed MD simulations of the

melting of CO<sub>2</sub> hydrate, performed at the University of Bergen, indicate  $d$  in the same range, although a dynamic broadening of the interface cannot be excluded (Fig. 4).

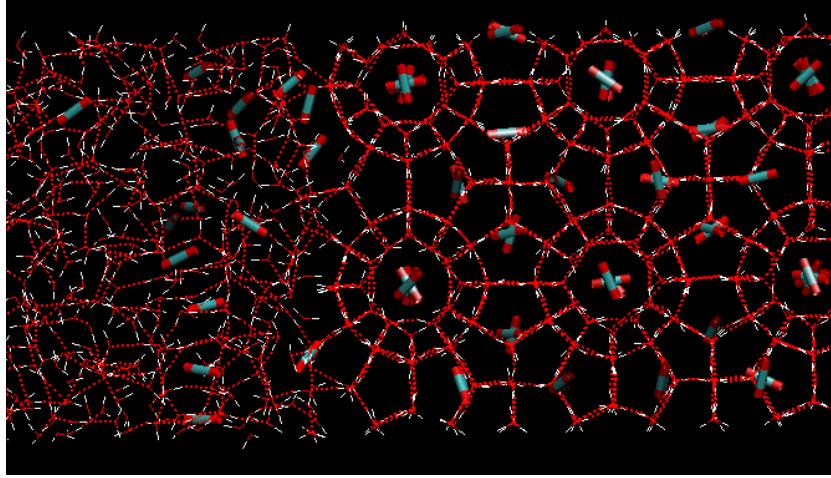


**Fig. 4** Snapshot of a molecular dynamics simulation on the melting of CO<sub>2</sub> hydrate in the presence of water. The simulation consists of 920 water and 108 CO<sub>2</sub> molecules (represented by SPC and EPM2 potentials, respectively), and has been performed at 276.15 K and 200 Bar. Note the regular clathrate cages inside the solid (on the right) and the distorted cages at the interface (on the left). The diameter of the H<sub>2</sub>O cages of circular projection (tetrakaidecahedra) is 0.866 nm. The rods at the center of the cages denote the CO<sub>2</sub> molecules. [This picture have been made using the Visual Molecular Dynamics package (Humphrey, W.; Dalke, A.; Schulten, K. J. *Molec. Graphics*, 1996, 14, 33).]

The computations are performed under conditions typical for the seabed reservoirs, i.e.  $T = 274$  K,  $p = 15$  MPa ( $\sim 1500$  m depth), furthermore, we assume that water has been saturated by CO<sub>2</sub> ( $c = 0.033$ , obtained by extrapolating the relevant data by Teng and Yamasaki [18]). These experimental data are for synthetic average seawater. The salinity of groundwater in reservoirs may vary from close to zero up to seawater salinity in regions where the penetration of seawater dominates the salinity.

In the 2D phase field simulations for CO<sub>2</sub> hydrate we used  $\varepsilon^2 = 1.3944 \times 10^{-15}$  J/cm K,  $w = 3.6372$  J/cm<sup>3</sup>K,  $D_l = 10^{-5}$  cm<sup>2</sup>/s,  $D_s = 0$ ,  $\xi = 10^{-8}$  cm,  $m_m = M_m \varepsilon^2 T / D_l = 4.4308$ , and  $\chi = 0.8381$ , while the time and spatial steps were  $\Delta t = 0.04 \tau$  and  $\Delta x = \xi$ , respectively. Simulations for confined space were done for Ni-Cu, using the properties given in [6,7,8].

## Results

### Hydrate nucleation

The thickness of the interface is estimated to be between 15 and 20 Ångströms. In order to compare the Phase Field simulations with the classical droplet theory, which exhibits a sharp interface of zero thickness we estimate the nucleation work for different interfacial thickness, ranging from 1.25 Å to 15 Å, at 274 K and 150 bar using a constant bulk concentration of CO<sub>2</sub> equal to 0.033 (solubility molefraction in water). The estimated nucleation work decreases almost linearly from  $3.61 \cdot 10^{-19}$  J for an interface thickness of 1.25 Å to  $2.23 \cdot 10^{-19}$  J for an interface thickness of 15 Å. For comparison the classical droplet model estimates  $3.76 \cdot 10^{-19}$  J, which extrapolates very well from the Phase Field results at 1.25 Å.

Remarkably, at the realistic interface thickness ( $d = 1.0$  to  $1.5$  nm) the bulk crystalline structure is not yet established even at the center of the nucleus, indicating that the nucleus is softer (the molecules have larger amplitude of oscillations around the crystal sites) than the bulk crystal. Despite these, we have almost full hole-occupancy in the central part,  $c = 0.1235$  or  $\theta = 0.946$ . Furthermore, the interface thickness for the concentration field is far sharper than for structure. It extends to only a few Å, which is

consistent with the picture that the nucleus is a small piece of hydrate crystal embedded into the solution, however, built of somewhat distorted H<sub>2</sub>O cages seen at the interface in MD simulations with realistic potentials (Fig. 1) [19]. It is remarkable, that the interface for the solute falls close to the classical radius  $R_{\text{CDM}}^* = 1.76 \text{ nm}$ .

We note finally, that the predicted  $W^*$  is rather sensitive to the values of  $\Gamma_\infty$  and  $d$  used to fix the model parameters  $\varepsilon$  and  $w$ . Thus, accurate results may only be expected if these input properties are known with a high accuracy. Unfortunately, none of them is available for the CO<sub>2</sub> hydrate/solution interface (the values used here and in other work [15] are only rough estimates). Therefore, further effort is needed to establish accurate nucleation rates. For example, careful experiments using the grain boundary groove method [16] could provide a reasonably accurate value for the interfacial free energy. Another possible way to determine the interfacial properties is via MD simulations [20,21] with realistic interaction potentials. Work is underway in these directions.

### ***Growth of CO<sub>2</sub> hydrate particles***

The growth of a supercritical CO<sub>2</sub> hydrate particle is simulated at the same condition and the results are plotted in fig. 5. The actual particle radius is defined as the point of growing front where  $m=0.5$ , i.e.: average particle size. The time-dependence indicates that, as expected, growth is governed here by CO<sub>2</sub> diffusion in the liquid.

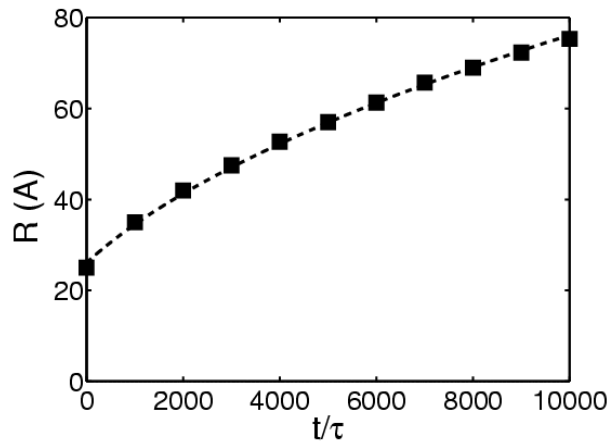


**Fig. 5** Radius of the CO<sub>2</sub> particle as a function of reduced time during the early growth stage in 2D. (Here  $\tau = 10^{-11} \text{ s}$ .) Dashed line denotes an  $R = [A(t - t_0)]^{1/2}$  function fitted to the  $R(t)$  relationship [ $A = (0.51 \pm 0.01) \times 10^{-5} \text{ cm}^2/\text{s}$  and  $t_0 = (-1328 \pm 58) \times 10^{-11} \text{ s}$ ]. The average growth rate for the period shown is  $\sim 5.3 \text{ cm/s}$ . Growth rate, however, slows down as  $v = (1/2)[A / (t - t_0)]^{1/2}$ , yielding  $\sim 11 \text{ }\mu\text{m/s}$  after 1 s, unless interaction with other particles or the morphological instability intervenes.

### ***Crystal growth in the presence of walls***

To study solidification in confined spaces walls are introduced into the PFT simulations. In our model, the “no-flux” boundary condition is used to realize a rectangular contact angle and a chemically inert wall. In the simulations, the orientation field can be either random [no preferred orientation (glassy wall)] or one may chose preferred orientation(s). The introduction of such walls allows the study of heterogeneous crystal nucleation on particles, rough surfaces, and crystallization in porous matter or in channels. Preliminary results obtained with ideal solution thermodynamics (Ni-Cu system) are shown in Figs. 6. A similar approach is yet being applied to the modelling of hydrate formation in confined geometries.

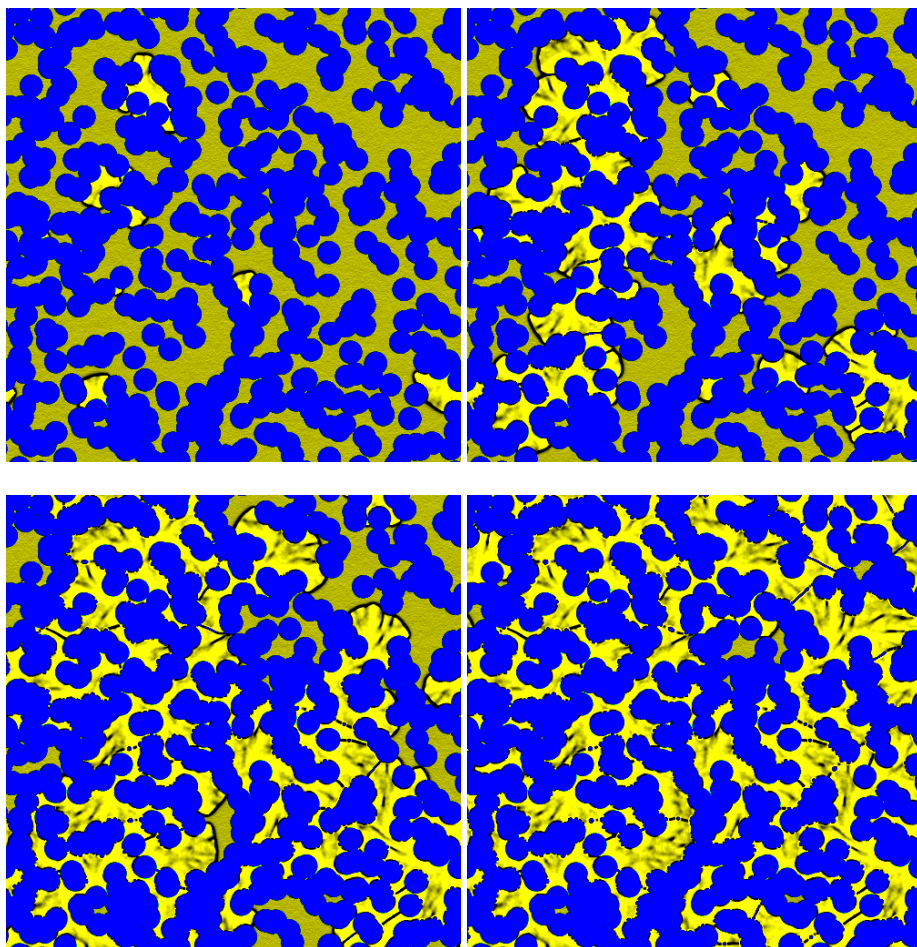


**Fig. 6** Solidification in porous matter. Blue – particles of porous matter, dark yellow – liquid, bright yellow – solid.

## Conclusions

Preliminary results showed that hydrate took several hours to form and formed according to gradually decreasing gas saturation from the gas injection face rather than in discrete areas. Permeability went to zero when less than half of the sample was filled with hydrate implying that selected, but not detected, areas were completely filled with hydrate before all of the pore volume was filled.

The nucleation and growth of CO<sub>2</sub> hydrate in aqueous solution is addressed using a phase field theory we developed recently. It has been demonstrated under typical conditions, that the thickness of the hydrate-solution interface is comparable with the size of nuclei. Apparently, advanced models are needed to evaluate the rate of hydrate nucleation accurately. The phase field theory is used to predict the growth rate of CO<sub>2</sub> hydrate in aqueous solution. The growth is governed by CO<sub>2</sub> diffusion in the liquid. We have introduced walls into the phase field simulations and demonstrated the possibility for modelling solidification in confined space (channels/porous media).

## Acknowledgments

This work has been supported by the Norsk Hydro, The Norwegian Research Council, ConocoPhillips, Hungarian Academy of Sciences under contract No. OTKA-T-037323 and by the Norwegian Research Council under project Nos. 153213/432 and 151400/210.

## References

1. Mienert, J., Univ. Of Tromsø, Norway, Private communication February 6, 2004
2. Kvamme, B, Graue, A., Aspenes, E., Kuznetsova, T., Gránásy, L., Tóth, G., Pusztai, T., Tegze G., Towards understanding the kinetics of hydrate formation: Phase field theory of hydrate nucleation and magnetic resonance imaging, *Physical Chemistry Chemical Physics*, 2003, in press
3. Granasy, L., Pusztai, T., Tegze, G., Kuznetsova, T., Kvamme, B., Phase field theory of hydrate nucleation: Formation of CO<sub>2</sub> hydrate in aqueous solution, in "Recent Advances in the Study of Gas Hydrates", 2004, Kluwer Academic/Plenum Publishers, in press
4. Davidchack, R. L.; Laird, B. B. *J. Chem. Phys.*, 1998, 108, 9452
5. Oxtoby, D. W. *Annu. Rev. Mater. Res.*, 2002, 32, 39
6. Gránásy, L.; Börzsönyi, T.; Pusztai, T. *Phys. Rev. Lett.*, 2002, 88, 206105.
7. Gránásy, L.; Börzsönyi, T.; Pusztai, T. *J. Cryst. Growth.*, 2002, 237-239, 1813.
8. Gránásy, L.; Pusztai, T.; Tóth, G.; Jurek, Z.; Conti, M; Kvamme, B. *J. Chem. Phys.* 2003, 119, 10376.
9. Gránásy, L.; Pusztai, T.; Warren, J. A.; Douglas, J. F.; Börzsönyi, T.; Ferreira, V. *Nature Mater.*, 2003, 2, 92.
10. Kobayashi, R., Warren, J. A.; Carter, W. C. *Physica D*, 1998, 119, 415
11. Warren, J. A.; Gránásy, L.; Pusztai, T.; Börzsönyi, T.; Tegze, G.; Douglas, J. F. *Proc. TMS Ann. Meeting*, San Francisco, 2004, accepted for publication
12. Kvamme, B. unpublished.
13. Stewart, P. B.; Munjal, P. J. *Chem. Eng. Data*, 1970, 15, 67.
14. Kvamme, B.; Tanaka, H. *J. Phys. Chem.*, 1995, 99, 7114
15. Kashchiev, D.; Firoozabadi, A. *J. Cryst. Growth*, 2002, 243, 476.
16. Hardy, S. C. *Philos. Mag.*, 1977, 35, 471.
17. Pratt, R. M.; Mei, D.-H.; Guo, T.-M.; Sloan, E. D. *J. Chem. Phys.*, 1997, 106, 4187
18. Teng, H.; Yamasaki, A. *J. Chem. Eng. Data*, 1998, 43, 2
19. Harris, J. G.; Yung, K. H. *J. Phys. Chem.*, 1995, 99, 12021
20. Hoyt, J. J.; Asta, M.; Karma, A. *Phys. Rev. Lett.*, 2001, 86, 5530
21. Davidchack, R. L.; Laird, B. B. *J. Chem. Phys.*, 1998, 108, 9452